PNAS

Main Manuscript for

Quantifying NO_x point sources with Landsat and Sentinel-2 satellite observations of NO_2 plumes

Daniel J. Varon[1]*, Dylan Jervis[2], Sudhanshu Pandey[3], Sebastian L. Gallardo[4], Nicholas Balasus[1], Laura H. Yang[1], Daniel J. Jacob[1]

[1] School of Engineering and Applied Sciences, Harvard University, Cambridge, United States.
[2] GHGSat, Inc., Montréal, Canada.
[3] Jet Propulsion Laboratory, California Institute of Technology, Pasadena, United States.
[4] Centro Atomico Bariloche, Bariloche, RN, Argentina.

*Corresponding author: Daniel J. Varon

Email: danielvaron@g.harvard.edu

Competing Interest Statement: The authors declare that they have no competing interests.

Classification: Physical Sciences.

Keywords: Nitrogen oxides, Point sources, Satellites, Remote Sensing.

This PDF file includes:

Main Text
Figures 1 to 4
Table 1

Abstract

We show that the Landsat and Sentinel-2 satellites can detect NO_2 plumes from large point sources at 10–60 m pixel resolution in their blue and ultra-blue bands. We use the resulting NO_2 plume imagery to quantify NO_x emission rates for several power plants in Saudi Arabia and the United States, including a 13-year analysis of 140 Landsat plumes from Riyadh power plant 9 from 2009 through 2021. NO_2 in the plumes initially increases with distance from the source, likely reflecting recovery from ozone titration. The fine pixel resolutions of Landsat and Sentinel-2 enable separation of individual point sources and stacks, including in urban background, and the long records enable examination of multidecadal emission trends. Our inferred NO_x emission rates are consistent with previous estimates to within a precision of about 30%. Sources down to ~500 kg h^{-1} can be detected over bright, quasi-homogeneous surfaces. The 2009–2021 data for Riyadh power plant 9 show a strong summer peak in emissions, consistent with increased power demand for air conditioning, and a marginal slow decrease following the introduction of Saudi Arabia's Ambient Air Standard 2012.

Significance Statement

Atmospheric nitrogen oxides (NO_x) are air pollutants with important implications for air quality, climate, and the biosphere. Satellites have mapped atmospheric NO_2 concentrations since the 1990s, but with spatial resolution generally too coarse to resolve individual point sources such as power plants. We show here that the Landsat and Sentinel-2 land-surveying satellites can map NO_2 plumes at 10–60 m resolution in their visible bands and quantify emissions from individual power plants, despite not having been designed for this purpose. Their high spatial resolution enables separation of individual point sources and stacks, and their long records, with global coverage every few days, enable analysis of multidecadal emission trends.

Introduction

Nitrogen oxides ($NO_x \equiv NO + NO_2$) play important roles in air quality, radiative forcing, and nitrogen deposition to the biosphere. Natural sources of NO_x include lightning, soils, and wildfires. Anthropogenic emissions are mainly from fossil fuel combustion by vehicles and large stationary point sources such as power plants. Dedicated satellite instruments measuring backscattered sunlight in the ultraviolet-visible (UV/Vis) spectral range have provided global mapping of atmospheric NO_2 concentrations since the 1990s to quantify NO_x emissions and trends, with pixel resolution down to 3.5×5.5 km^2 for the highest-resolution TROPOMI instrument launched in 2017 (Veefkind et al., 2012). This is generally too coarse to resolve individual NO_x point sources except for large, isolated facilities and/or using extensive temporal averaging (Beirle et al., 2019; 2021; 2023; Georgoulias et al., 2020; Godlowska et al., 2023; Hakkarainen et al., 2023). Here we demonstrate the ability of the Landsat and Sentinel-2 satellites to quantify strong NO_x point sources at 10–60 m pixel resolution with single-pass observations and thus monitor facility-level emissions and trends, including in urban background.

Landsat (Irons et al., 2012) and Sentinel-2 (Drusch et al., 2012) are global land-surveying satellite missions for monitoring terrestrial resources and land use. Landsat has provided continuous global coverage since the launch of Landsat 1 in 1972, with Landsat 8 (2013–present) and Landsat 9 (2021–present) forming the current operational constellation. The Landsat satellites are in near-polar sun-synchronous orbit with a 10:00–10:30 equatorial crossing time on the descending node. Each carries an Operational Land Imager (OLI) with 185 km swath, 15–30 m pixel resolution, and 9 spectral channels ranging from the visible to shortwave infrared. Together, Landsat 8 and 9 provide global coverage every 8 days. Sentinel-2 comprises a pair of satellites, Sentinel-2A (2015–present) and Sentinel-2B (2017–present), in polar sun-synchronous orbit with a ~10:30 equatorial crossing time. Their MultiSpectral Instruments (MSI) observe in 13 spectral channels from the visible to shortwave infrared, with 10–60 m spatial resolution across a 290 km swath. Together, the Sentinel-2 satellites scan the globe every 5 days.

Here we show how one can use the blue (B) and ultra-blue (UB) bands of the Landsat OLI and Sentinel-2 MSI to map NO_2 plumes at 10–60 m pixel resolution and quantify individual NO_x point sources. The shortwave infrared bands have previously been used to identify methane plumes (Varon et al., 2021; Ehret et al., 2022). We focus on large power plants in scenes with favorable (bright and/or quasi-homogeneous) surface conditions, but also demonstrate the ability to resolve point sources over darker surfaces and against the backdrop of urban NO_x emissions. We present a long-term record of emissions from a large oil- and gas-fired power plant near Riyadh, Saudi Arabia using 140 plumes detected over 13 years from 2009 through 2021.

Results

Figure 1 shows a selection of NO_2 plumes from power plants in Saudi Arabia and the United States, as observed by Landsat and Sentinel-2. The scenes are generally bright, with surface types ranging in complexity from remote desert (Fig. 1b, c) to urban mosaic (Fig. 1a) and semi-arid steppe (Fig. 1d). The retrievals use different instruments and spectral bands to illustrate the range of options available; NO_2 sensitivity is highest in the ultra-blue band, but Sentinel-2's blue band offers finer pixel resolution (Materials and Methods). Inventory estimates from the Global Power Emission Database (GPED; Tong et al., 2018) and previous TROPOMI-based estimates provide independent evaluation of our estimated source rates. We selected the power plants of Figure 1 as test cases based on previous reports of strong emissions from GPED and/or remote sensing. Strong NO_x emissions from power plants in Riyadh (Fig. 1a, b) have been documented by OMI (Valin et al., 2013) and TROPOMI (Beirle et al., 2019); the Qurayyah power plants (Fig. 1c) are together the highest-emitting Saudi Arabian gas plants in the GPED inventory; and Cusworth et al. (2021) previously mapped the CO_2 plume from the Bridger power plant (Fig. 1d) on the date we examine here using aerial remote sensing.

Figure 1a shows an NO_2 plume from Riyadh power plant 8 (24.597°N, 46.572°E; top-right of image) detected by Sentinel-2 on 4 July 2020. Riyadh 8 is a 2.1 gigawatt (GW) natural gas and diesel power plant. We estimate a single-pass NO_x emission of 1030 kg h^{-1} for the plant using a cross-sectional flux method (Materials and Methods). This is lower than the temporal mean

estimates of 2050 kg h^{-1} from GPED for 2010 and 1690 ± 710 kg h^{-1} as reported by Beirle et al. (2019) from analysis of TROPOMI data for the December 2017 to October 2018 period using the divergence method (Materials and Methods). The Sentinel-2 plume is clearly detectable despite the surface variability of the urban scene (roads, buildings).

Figure 1b shows a Sentinel-2 detection of the NO_2 plume from Riyadh power plant 9 (24.950°N, 47.065°E) on 26 June 2021. Riyadh 9 is a 1.7 GW power plant fueled by crude oil, natural gas, and diesel. It is located about 50 km east of Riyadh. NO_x emissions from the plant are large and routinely detectable over its bright and uniform surroundings. The sample observation shown in Figure 1b demonstrates the ability of Sentinel-2 to resolve emissions from individual power plant exhaust stacks using the blue band with 10-m pixel resolution. For this detection we estimate a total NO_x emission of 2940 kg h^{-1} for the plant. We present below the 13-year history of Riyadh 9 NO_x emissions from 2009-2021 as observed by Landsat 7 and Landsat 8, including detailed comparison with previous estimates.

Figure 1c shows two large NO_2 plumes from power plants in the eastern Qurayyah province of Saudi Arabia, detected by Landsat 8 on 17 October 2021. Qurayyah I and II are among the largest gas-fired power plants in the world at 3.9 GW and 3.8 GW, respectively, and are located less than 3 km apart. Landsat can separate the individual plumes, but TROPOMI could not. We find single-pass emissions of 1450 kg h^{-1} for Qurayyah I to the north and 1160 kg h^{-1} for Qurayyah II to the south, similar to the combined GPED estimate of 3310 kg h^{-1}.

Figure 1d shows an NO_2 plume from the 2.4 GW Jim Bridger coal-fired power plant in Wyoming, USA, detected by Landsat 8 on 1 August 2020. NO_x plumes from US power plants are not easily detectable by Landsat and Sentinel-2 due to widespread use of NO_x emission controls. The Bridger power plant is outfitted with low-NO_x burner technology. Of 11 clear-sky Landsat 8 passes free of condensed water vapor plumes in 2020, we detect only one NO_2 plume from the power plant, at 11:55 local time on 1 August 2020, under low-wind conditions; the 500-m wind U_{500} was 2.0 m s^{-1} according to the NASA Goddard Earth Observing System Fast Processing (GEOS-FP) meteorological product (Molod et al., 2012). The US EPA Clean Air Markets Program Database (CAMPD) reports NO_x emissions of 740 kg h^{-1} for that hour from the Bridger Continuous Emission Monitoring System (CEMS). We estimate 550 kg h^{-1} from Landsat 8, which may reflect a low bias from ozone titration (discussed below). NO_x is mainly emitted as NO, and conversion to NO_2 in the fresh plume from oxidation by ozone may be delayed if ozone is titrated (Sykes et al., 1992). The plume starts to be detectable a few hundred meters downwind of the exhaust stacks, likely also due to ozone titration. The Bridger case demonstrates that relatively low NO_x emissions can be detected in complex scenes if winds are low and if a good reference scene for the retrieval is available (here 17 August 2020; Materials and Methods).

Table 1 summarizes the comparisons of our source rate results with previous estimates for the five power plants of Figure 1. Our estimates show a mean low bias of 25%, likely reflecting delayed NO_2 formation in the fresh plume due to ozone titration. The mean absolute deviation between estimates is about 30%, and we take this to represent a lower limit on the source rate retrieval precision. An error standard deviation of 30% or more is consistent with what one would expect from uncertainty in the wind speed (Varon et al., 2018) and NO_x/NO_2 ratio (Beirle et al., 2023).

Figure 2 shows normalized NO_2 fluxes as a function of distance downwind from the power plant for the five plumes of Figure 1. In all cases, the NO_2 cross-sections tend to grow with distance downwind, which we attribute to gradual recovery from ozone titration as background ozone is entrained into the diluting plume. None of the plumes show an eventual decrease downwind that would reflect NO_x oxidation, and that may be explained by the short aging times (~10 minutes) relative to the lifetime of NO_x against oxidation (~1 hour). By contrast, much larger and coarsely resolved OMI and TROPOMI plumes show declining NO_2 with distance from the source due to NO_x oxidation (Valin et al., 2013; Laughner and Cohen, 2019). The Riyadh 8 and Qurayyah plumes show early recovery from ozone titration followed by steady NO_2 fluxes, while the Riyadh 9 and Bridger plumes suggest delayed recovery and our source rate estimate would then be a lower limit.

Figure 3 shows a 13-year history of NO_x emissions from Riyadh power plant 9 based on 2009–2021 Landsat observations. We quantified a total of 140 plumes in cloud-free scenes over this period, including 30 from Landsat 7 (2009–2013) and 110 from Landsat 8 (2013–2021). We only consider passes for which the GEOS-FP 10-m wind U_{10} > 2 m s^{-1} to exclude observations with

uncertain wind direction when selecting reference scenes for the retrieval (Materials and Methods). Landsat 7 shows sparser detections than Landsat 8 because its retrievals are significantly noisier due to an instrument failure in 2003 that led to the loss of about 25% of image pixels. We therefore consider Landsat 7 data only before Landsat 8 became operational in March 2013. Plumes were clearly detectable in 76% of Landsat 8 passes. Non-detections cannot generally be assumed to reflect low or null emissions because the retrieval precision and corresponding detection limit can vary strongly from pass to pass with the quality of the best available reference scene. The period-average values reported below are therefore based only on detected plumes.

We find that NO_x emissions from the power plant averaged 2970 ± 1960 kg h^{-1} (mean ± standard deviation) from 2009–2021. Our mean NO_x emission estimate for the year 2010 is 1920 ± 660 kg h^{-1}, higher than the GPED value of 1130 kg h^{-1}. Beirle et al. (2019) reported a mean emission of 2230 kg h^{-1} for December 2017 to October 2018, and we obtain 2750 ± 1090 kg h^{-1} for that period. Beirle et al. (2023) made several improvements to their earlier methods, including better estimates of NO_x/NO_2 ratios (which we implement here) and NO_x chemical lifetime, and reported an updated mean estimate of 3900 kg h^{-1} for the year 2018, 40% higher than our 2750 kg h^{-1} estimate. This may be due in part to diurnal variability in power generation if emissions are higher during afternoon TROPOMI passes (~13:00 local time) than morning Landsat passes (~10:15 local time) due to increased air conditioning (AC) power demand. Such diurnal emission variability has previously been observed for power plants in the United States (Boersma et al., 2008; Kim et al., 2009) and Qatar (Rey-Pommier et al., 2023).

Landsat infers strong seasonal variability in emissions from Riyadh power plant 9, with much higher levels during summer than winter, again likely due to AC power demand. Saudi Arabia introduced new air quality standards in March 2012 (Ambient Air Standard 2012). Our retrievals show that NO_x emissions spiked that summer and averaged 3100 kg h^{-1} through 2021, with a weak decreasing trend of –140 [–310, 30] kg h^{-1} per year (p = 0.08) in the 2013–2021 annual mean based on Landsat 8. The 50% increase from the pre-2012 average of 2010 kg h^{-1} may reflect increased power generation at Riyadh power plant 9 to offset decreased generation elsewhere, and the gradual post-2012 decline may reflect improvement in pollution control technology.

Discussion

Our work demonstrates the detection and quantification of strong NO_x point sources with Landsat and Sentinel-2 multispectral satellite observations. We used the instruments' blue and ultra-blue bands to map NO_2 plumes from individual power plants at 10–60 m resolution and infer source rates, focusing on a few large Saudi Arabian and US facilities. The NO_2 plumes we examined tended to grow downwind, likely reflecting recovery from ozone titration and demonstrating the potential to characterize the chemical dynamics of individual NO_x point source plumes from space. The source rates we estimated with Sentinel-2 and Landsat are consistent with previous estimates to within a precision of about 30%, but biased low by ~25% due to ozone titration in the fresh plume. Our 13-year analysis of NO_2 plumes from Riyadh power plant 9 illustrates how Landsat (1972–present) can enable both seasonal and multidecadal monitoring of emissions and trends for individual NO_x point sources.

The limitations of Landsat and Sentinel-2 NO_2 retrievals must be recognized. The retrievals are most successful over bright homogeneous surfaces. Over these surfaces, a source rate detection limit of about 500 kg NO_2 h^{-1} can be inferred from the consistent detection of emissions from Riyadh power plant 9, for which our lowest source rate estimate was 350 kg h^{-1}. Identifying a good reference scene to remove albedo-related artifacts is more challenging for complex surfaces, but we were able to sporadically detect plumes over darker surfaces (Bridger) and an urban mosaic (Riyadh 8). Additionally, the retrievals cannot be applied to scenes containing large aerosol plumes, such as condensed water vapor in cold conditions or carbon particles in poorly performing combustion systems.

Quality of the reference scenes is presently the main factor limiting our ability to observe NO_2 plumes with Landsat and Sentinel-2. This could be addressed in the future by applying statistical learning to the long data records. Precision in the inferred source rates may be limited by uncertainty in wind speed (Varon et al., 2018). Low bias from ozone titration could be addressed by tracking the plumes further downwind in adjacent tiles, considering that in all cases of Figure 1

the plumes exit the tile before they have dissipated to below the detection limit (Materials and Methods). Mining of the Landsat and Sentinel-2 global records would give a better characterization of detection limits and enable better comparison to the large TROPOMI point source dataset developed by Beirle et al. (2023). It may be possible to extend the Landsat/Sentinel-2 NO_2 capability to other multispectral Earth observation satellites with coarse UV/Vis spectral bands, including instruments in low-Earth orbit with up to daily revisits (e.g., Sentinel-3, MODIS) and in geostationary orbit with up to 5-minute revisits (e.g., GOES, Himawari-8), though many of these instruments have coarser pixel resolution. Hyperspectral surface mapping instruments such as EMIT (Green et al., 2020), PRISMA (Cogliati et al., 2021), and EnMAP (Guanter et al., 2015) have ultra-blue bands with ~10 nm spectral resolution that should enable better quantification of NO_x point sources (Joiner et al., 2023), albeit with lower spatiotemporal coverage than Landsat and Sentinel-2.

Materials and Methods

The Landsat and Sentinel-2 top of atmosphere data for this study are available through Google Earth Engine (https://earthengine.google.com; Gorelick et al., 2017). The GEOS-FP and MERRA-2 wind data are available through the NASA Climate Data Services portal (https://www.nccs.nasa.gov/services/climate-data-services; Molod et al., 2012). The HITRAN line spectra are available through the HITRANonline database (https://hitran.org/; Gordon et al., 2017).

Sentinel-2 and Landsat data

Our NO_2 retrievals use top-of-atmosphere (TOA) reflectances in the Landsat and Sentinel-2 visible bands. We retrieve the reflectance data from Google Earth Engine (GEE; Gorelick et al., 2017) for image tiles of size 6 × 6 km^2 to 7.5 × 7.5 km^2, centered on a site of interest. The tile size is limited by the maximum number of pixels that can be retrieved automatically from GEE. The reflectance tiles are delivered along with metadata for acquisition time and viewing/solar zenith angles. Landsat OLI and Sentinel-2 MSI provide four visible bands in the ultra-blue (UB, ~430–450 nm), blue (B, ~450–530 nm), green (G, ~530–590 nm), and red (R, ~640–680 nm). Landsat 7 and earlier provide only the red, green, and blue (RGB) bands. The Landsat visible bands all have 30-m pixel resolution. The Sentinel-2 RGB bands have 10-m pixel resolution, but the UB band has 60-m resolution. Our retrievals make use of the B and UB bands to quantify NO_2 column concentrations. The UB band samples stronger NO_2 absorption lines (Fig. 4) and falls within the spectral range used by TROPOMI and other atmospheric sensors for NO_2 retrievals (Bucsela et al., 2006; 2013; van Geffen et al., 2022). We use it exclusively for our Landsat 8 retrievals. We use the B band for Landsat 7, which does not have a UB band, and both bands for Sentinel-2 where they have distinct advantages (stronger absorption for UB, but finer pixel resolution for B).

Figure 4 shows optical depths of NO_2, water vapor, and ozone in the 300–700 nm UV/Vis spectral range, along with Landsat 8 bands 1–4. The optical depths are based on absorption cross-sections from Vandaele et al. (1998) for NO_2, the HIgh-resolution TRANsmission molecular absorption (HITRAN2016) database (Gordon et al., 2017) for water vapor, and Gorshelev et al. (2014) and Serdyuchenko et al. (2014) for ozone, applied to vertical concentration profiles from the US Standard Atmosphere (Anderson et al., 1986). Most of the information on NO_2 absorption is contained in bands 1 and 2 (UB and B), which have much higher mean optical depths than the other bands (47 times higher in band 1 than in band 4). NO does not have strong absorption features in these bands.

NO_2 column retrievals

Our retrievals infer NO_2 column enhancements (mol m^{-2}) by comparing UB/B reflectances in a scene of interest ("target scene") with a reference either from the R/G bands for that same scene or from the UB/B bands for one or more plume-free reference scenes. The presence of an NO_2 plume can then be inferred from differences between target and reference. The reference scene should have similar surface features to the target scene but no NO_2 enhancements. As described

by Varon et al. (2021) for Sentinel-2 methane retrievals, we tried three different approaches to defining the reference; the same band on multiple passes (single-band–multi-pass retrieval, SBMP), multiple bands on the same pass (multi-band–single-pass retrieval, MBSP), and a combination of the two (multi-band–multi-pass retrieval, MBMP). We obtained the best results with SBMP retrievals, limiting our attention to the UB and B bands. We focus on those results here.

For a target scene on pass i and reference scene on pass j, we compute the normalized reflectance ratio in a band k (UB or B) as

$$r_k = \frac{c_k R_{i,k}}{R_{j,k}}. \quad (1)$$

Here R represents the observed top-of-atmosphere reflectance in the band of choice and c is a scale factor to remove scene-wide reflectance offsets in that band between passes, which could arise from surface and/or atmospheric conditions (e.g., temporal variations in surface albedo or water vapor absorption) or from changes in the sun-satellite configuration. Following Varon et al. (2021), we compute c for individual clear-sky scenes by linear regression of all R_j values onto all R_i values across the scene. We perform the regression after removing water pixels via the Normalized Difference Water Index (NDWI; McFeeters 1996).

Identifying a suitable reference scene for persistent NO_x point sources (e.g., power plants) requires knowledge of wind direction. We use 10-m wind direction data for individual scenes from the NASA Goddard Earth Observing System Fast Processing (GEOS-FP) product at 0.25° × 0.3125° resolution for passes after 20 February 2014 (when the GEOS-FP record begins), and the GEOS Modern-Era Retrospective Analysis for Research and Applications, version 2 (MERRA-2) product at 0.5° × 0.625° resolution for earlier passes. To prevent plume overlap between target and reference scenes, which would attenuate retrieved NO_2 enhancements, we require wind direction in the two scenes to differ by at least 60°. Wind direction can be highly uncertain under low wind conditions (Varon et al., 2020), hence we only consider scenes with 10-m wind speed $U_{10} > 2$ m s^{-1}. Ehret et al. (2022) found that Sentinel-2 methane retrieval artifacts can be reduced by using a linear combination of reference scenes rather than just one, so here we select 1–5 references for each target. The number of references is selected manually for each retrieval, and the passes themselves are selected automatically to maximize similarity with the target, which we evaluate from the root-mean-square error between the R band of the target pass and all other passes within a year of it.

We use the Beer-Lambert law assuming an optically thin plume to infer NO_2 slant column enhancements $\Delta\Omega$ (mol m^{-2}) from r_k as

$$\Delta\Omega = -\frac{\ln(r_k)}{\sigma_k}, \quad (2)$$

where σ_k (m^2 mol^{-1}) is the band averaged NO_2 absorption cross-section in band k (blue or ultra-blue) based on spectroscopic measurements by Vandaele et al. (1998) at 220K. To account for higher atmospheric temperatures, we apply a temperature correction to the retrieved columns following van Geffen et al. (2022). The correction assumes NO_2 plume enhancements are in the lowest 1000 m of the atmosphere and is based on the 500 m air temperature from GEOS-FP or MERRA-2.

We convert the retrieved slant columns to vertical columns $\Delta\Omega_v$ (mol m^{-2}) through a scattering air mass factor (AMF):

$$\Delta\Omega_v = \Delta\Omega/\mathrm{AMF}. \quad (3)$$

The AMF describes the light path as a function of the sun-satellite geometry and the scattering by the surface and atmosphere. It is computed as (Palmer et al., 2001):

$$\mathrm{AMF} = \mathrm{AMF}_G \int_{\mathrm{plume}} w(z)S(z)dz, \quad (4)$$

where $\mathrm{AMF}_G = \sec(\theta_s) + \sec(\theta_v)$ is the geometric AMF that depends only on the solar (θ_s) and viewing (θ_v) zenith angles; $w(z)$ is a wavelength-dependent scattering weight that describes the

signal attenuation from the atmosphere above height z with $w(z) = 1$ for a non-scattering atmosphere; $S(z) = \Delta n(z)/\Delta\Omega_{\mathrm{v}}$ is a normalized vertical shape profile for the NO_2 number density enhancement $\Delta n(z)$; and the integration is over the depth of the NO_2 plume. We assume $S(z)$ for the NO_2 plume to be a step function for the lowest km of the atmosphere so that the AMF can be approximated as

$$\mathrm{AMF} \approx \mathrm{AMF}_G\, w(h). \tag{5}$$

with $h = 500$ m. We take $w(h)$ from a look-up table of scattering weights for the OMI NO_2 satellite instrument with spectral fitting window of 405–465 nm, as a function of surface pressure, albedo, θ_s, θ_v, and the relative azimuth angle (RAA) between sun and satellite (Lamsal et al., 2021). We obtain θ_s, θ_v, and RAA from the satellite metadata. For each Landsat or Sentinel-2 scene, we obtain surface pressure from GEOS-FP or MERRA-2, and albedo (Lambertian-equivalent reflectance from 405–465 nm) from the nearest 0.25° × 0.25° grid cell of the OMI level-2 daily gridded retrieval product (Krotkov et al., 2019). Values of $w(h)$ range from 0.6 to 1 for our collection of scenes.

The spectral range of the OMI scattering weight look-up table (405–465 nm) contains the Landsat/Sentinel-2 UB bands (~435–450 nm) but only partially overlaps the instruments' B bands (~450–520 nm). Using the look-up table in B-band retrievals for Landsat-7 and Sentinel-2 would bias the NO_2 columns high by underestimating the mean scattering weight and thus underestimating AMF. We account for this by using Landsat-8, with 30-m resolution in both B and UB bands, to characterize the bias between retrievals in the two bands. In a selection of six retrievals from different sites and times of year, we find mean UB:B NO_2 ratios of 0.6 to 0.75. We take 0.66 as a representative intermediate value, consistent with the expected B:UB ratio of Rayleigh scattering weights between the two bands, and correspondingly scale down our B retrievals to apply the correction.

Source rate retrieval

Quantification of NO_x point sources with satellite observations was previously done by mass balance or fitting a Gaussian plume model to time averages of retrieval scenes from OMI (Ghude et al., 2013; de Foy et al., 2015) and TROPOMI (Zhang et al., 2019; Fioletov et al., 2022). Beirle et al. (2019) introduced a flux-divergence approach to quantify point sources directly from TROPOMI NO_2 observations and two-dimensional reanalysis winds, and Beirle et al. (2021; 2023) applied this to construct a global catalog of large NO_x point sources. These analyses examined very large plumes extending over tens of km and accounted for loss of NO_x by oxidation within the plume.

Here we seek to quantify emissions from single-pass satellite observations of turbulent NO_2 plumes at ≤ 30 m pixel resolution and extending over scenes only a few km across, corresponding to a plume aging time of the order of 10 minutes. This requires a different source rate retrieval because the instantaneous plumes cannot be assumed Gaussian and because the flux divergence approach fails at sub-km scales in absence of direct wind measurements around the divergence contour (Varon et al., 2018). Ozone titration in the fresh plume would delay conversion of emitted NO to NO_2 (Sykes et al., 1992). NO_x oxidation is not expected to be significant on the short time scales considered here.

Our approach is to use a cross-sectional flux (CSF) method to quantify the evolution of NO_2 fluxes in the plume as a function of distance downwind of the source, thus tracking the effects of both ozone titration and NO_x oxidation. The CSF method (Krings et al., 2013; Varon et al., 2018) applied to an NO_2 column retrieval field $\Delta\Omega_{\mathrm{v}}$ [mol m^{-2}] computes the NO_2 flux $F(x)$ [kg NO_2 h^{-1}] at a distance x downwind of the source as the product of the cross-plume integral column transect C [mol m^{-1}] and representative wind speed U [m s^{-1}]:

$$F(x) = M_{\mathrm{NO2}}\ U \int_a^b \Delta\Omega_{\mathrm{v}}\,(x,y)dy = M_{\mathrm{NO2}}\ U\ C, \tag{6}$$

where y is the cross-plume direction perpendicular to the plume axis x, $M_{\mathrm{NO2}} = 0.046$ kg mol^{-1} is the NO_2 molecular weight, and a and b are plume boundaries defined from a binary plume mask distinguishing plume from background. We take U to be the 500-m wind speed U_{500} from GEOS-FP or MERRA-2. We define the orientation of the cross-plume axis y by inspection of the plume, from a weighted average of pixel coordinates with the masked NO_2 enhancements as weights (Varon et al., 2018). We build the binary plume mask by applying a Gaussian filter with a 1–3-pixel kernel to the retrieved columns and then thresholding at the 75th–90th percentile, similar to the approach of Varon et al. (2019) for methane plumes.

Results presented in Figure 2 show that $F(x)$ initially increases with distance downwind of the source, which we attribute to ozone titration (Sykes et al., 1992). The plumes are too short to detect a decrease of $F(x)$ attributable to NO_x oxidation. We take the mean of the five highest values of $F(x)$ along the plume axis (F_{max}) as our best estimate of the source rate Q [kg NO_x h^{-1} as NO_2]:

$$Q = \alpha\, F_{\mathrm{max}}, \tag{7}$$

where α [mol mol^{-1}] is the NO_x/NO_2 concentration ratio in the plume at the distances downwind where F_{max} is calculated. We assume $\alpha = 1.38$ mol mol^{-1} as representative of the plume air after it has recovered from ozone titration (Beirle et al., 2023). The NO_x source rate is expressed in equivalent kg NO_2 to follow standard practice in the emission inventory community.

Acknowledgments

Work at Harvard was supported by GHGSat Inc. and by the Samsung Advanced Institute of Technology.

References

Anderson, G., Clough, S., Kneizys, F., Chetwynd, J., and Shettle, E.: AFGL atmospheric constituent profiles (0–120 km), Tech. Rep. AFGL-TR-86-0110, Air Force Geophys. Lab., Hanscom Air Force Base, Bedford, Mass., USA, 1986.

Beirle, S., Boersma, K. F., Platt, U., Lawrence, M. G., and Wagner, T.: Megacity emissions and lifetimes of nitrogen oxides probed from space, Science, 333, 1737–1739, https://doi.org/10.1126/science.1207824, 2011.

Beirle, S., Borger, C., Dörner, S., Li, A., Hu, Z., Liu, F., Wang, Y. and Wagner, T.: Pinpointing nitrogen oxide emissions from space, Sci. Adv., 5, eaax9800, https://doi.org/10.1126/sciadv.aax9800, 2019.

Beirle, S., Borger, C., Dörner, S., Eskes, H. J., Kumar, V., De Laat, A., and Wagner, T.: Catalog of NOx emissions from point sources as derived from the divergence of the NO2 flux for TROPOMI, Earth Syst. Sci. Data, 13, 2995–3012, https://doi.org/10.5194/essd-13-2995-2021, 2021.

Beirle, S., Borger, C., Jost, A., and Wagner, T.: Improved catalog of NOx point source emissions (version 2), Earth Syst. Sci. Data, 15, 3051–3073, https://doi.org/10.5194/essd-15-3051-2023, 2023.

Boersma, K. F., Jacob, D. J., Eskes, H. J., Pinder, R. W., Wang, J., and van der A, R. J.: Intercomparison of SCIAMACHY and OMI tropospheric NO2 columns: Observing the diurnal evolution of chemistry and emissions from space, 113, D16S26, https://doi.org/10.1029/2007JD008816, 2008.

Bovensmann, H., Burrows, J. P., Buchwitz, M., Frerick, J., Noël, S., Rozanov, V. V., Chance, K. V., and Goede, A. P. H.: SCIAMACHY: Mission Objectives and Measurement Modes, J. Atmos. Sci., 56, 127–150, https://doi.org/10.1175/1520-0469(1999)056<0127:SMOAMM>2.0.CO;2, 1999.

Bucsela, E. J., Celarier, E. A., Wenig, M. O., Gleason, J. F., Veefkind, J. P., Boersma, K. F., and Brinksma, E. J.: Algorithm for NO2 vertical column retrieval from the ozone monitoring instrument, IEEE T. Geosci. Remote, 44, 1245–1258, https://doi.org/10.1109/TGRS.2005.863715, 2006.

Bucsela, E. J., Krotkov, N. A., Celarier, E. A., Lamsal, L. N., Swartz, W. H., Bhartia, P. K., Boersma, K. F., Veefkind, J. P., Gleason, J. F., and Pickering, K. E.: A new stratospheric and tropospheric NO2 retrieval algorithm for nadir-viewing satellite instruments: applications to OMI, Atmos. Meas. Tech., 6, 2607–2626, https://doi.org/10.5194/amt-6-2607-2013, 2013.

Burrows, J. P. and Chance, K. V.: SCIAMACHY and GOME: The scientific objectives, Optical Methods in Atmospheric Chemistry, 1715, 502–512, https://doi.org/10.1117/12.140201, 1993.

Cogliati, S., Sarti, F., Chiarantini, L., Cosi, M., Lorusso, R., Lopinto, E., Miglietta, F., Genesio, L., Guanter, L., Damm, A., P´erez-Lopez, ´ S., Scheffler, D., Tagliabue, G., Panigada, C., Rascher, U., Dowling, T., Giardino, C., Colombo, R., 2021. The prisma imaging spectroscopy mission: overview and first performance analysis. Remote Sens. Environ. 262, 112499. https://www.sciencedirect.com/science/article/pii/S0034425721002170.

de Foy, B., Lu, Z., Streets, D. G., Lamsal, L. N., & Duncan, B. N. (2015). Estimates of power plant NOx emissions and lifetimes from OMI NO2 satellite retrievals. Atmospheric Environment, 116, 1–11.

Drusch, M., Del Bello, U., Carlier, S., Colin, O., Fernandez, V., Gascon, F., Hoersch, B., Isola, C., Laberinti, P., Martimort, P., Meygret, A., Spoto, F., Sy, O., Marchese, F., and Bargellini,

P.: Sentinel-2: ESA's Optical High-Resolution Mission for GMES Operational Services, Remote Sens. Environ., 120, 25–36, https://doi.org/10.1016/j.rse.2011.11.026, 2012.

Ehret, T., De Truchis, A., Mazzolini, M., Morel, J.-M., D'aspremont, A., Lauvaux, T., Duren, R., Cusworth, D., and Facciolo, G.: Global tracking and quantification of oil and gas methane emissions from recurrent sentinel-2 imagery, Environ. Sci. Technol., 355 56, 10517–10529, https://doi.org/10.1021/acs.est.1c08575, 2022.

European Space Agency (ESA): Sentinel-2 MSI Technical Guide. Available at https://sentinel.esa.int/web/sentinel/technical-guides/sentinel-2-msi/msi-instrument, 2023.

Fioletov, V., McLinden, C. A., Griffin, D., Krotkov, N., Liu, F., and Eskes, H.: Quantifying urban, industrial, and background changes in NO2 during the COVID-19 lockdown period based on TROPOMI satellite observations, Atmos. Chem. Phys., 22, 4201–4236, https://doi.org/10.5194/acp-22-4201-2022, 2022.

Georgoulias, A. K., Boersma, K. F., Van Vliet, J., Zhang, X., Van Der A, R., Zanis, P., and De Laat, J.: Detection of NO2 pollution plumes from individual ships with the TROPOMI/S5P satellite sensor, Environ. Res. Lett., 15, 124037, https://doi.org/10.1088/1748-9326/abc445, 2020.

Ghude, S. D., Kulkarni, S. H., Jena, C., Pfister, G. G., Beig, G., Fadnavis, S., & van der A, R. J.(2013). Application of satellite observations for identifying regions of dominant sources of nitrogen oxides over the Indian Subcontinent. Journal of Geophysical Research: Atmospheres, 118, 1075–1089. https://doi.org/10.1029/2012JD017811

Godłowska, J., Hajto, M. J., Lapeta, B., and Kaszowski, K.: The attempt to estimate annual variability of NOx emission in Poland using Sentinel-5P/TROPOMI data, Atmos. Environ., 294, 119482, https://doi.org/10.1016/j.atmosenv.2022.119482, 2023.

Gordon, I. E., Rothman, L. S., Hill, C., Kochanov, R. V., Tan, Y., Bernath, P. F., Birk, M., Boudon, V., Campargue, A., Chance, K. V., Drouin, B. J., Flaud, J.-M., Gamache, R. R., Hodges, J. T., Jacquemart, D., Perevalov, V. I., Perrin, A., Shine, K. P., Smith, M.-A. H., Tennyson, J., Toon, G. C., Tran, H., Tyuterev, V. G., Barbe, A., Császár, A. G., Devi, V. M., Furtenbacher, T., Harrison, J. J., Hartmann, J.-M., Jolly, A., Johnson, T. J., Karman, T., Kleiner, I., Kyuberis, A. A., Loos, J., Lyulin, O. M., Massie, S. T., Mikhailenko, S. N., Moazzen-Ahmadi, N., Müller, H. S. P., Naumenko, O. V., Nikitin, A. V., Polyansky, O. L., Rey, M., Rotger, M., Sharpe, S. W., Sung, K., Starikova, E., Tashkun, S. A., Auwera, J. V., Wagner, G., Wilzewski, J., Wcisło, P., Yu, S., and Zak, E. J.: The HITRAN2016 Molecular Spectroscopic Database, J. Quant. Spectrosc. Radiat. Transf., 203, 3–69, https://doi.org/10.1016/j.jqsrt.2017.06.038, 2017.

Gorelick, N., Hancher, M., Dixon, M., Ilyushchenko, S., Thau, D., and Moore, R.: Google Earth Engine: Planetary-scale geospatial analysis for everyone. Remote Sensing of Environment, https://doi.org/10.1016/j.rse.2017.06.031, 2017.

Gorshelev, V., Serdyuchenko, A., Weber, M., Chehade, W., and Burrows, J. P.: High spectral resolution ozone absorption cross-sections – Part 1: Measurements, data analysis and comparison with previous measurements around 293 K, Atmos. Meas. Tech., 7, 609–624, https://doi.org/10.5194/amt-7-609-2014, 2014.

Green, Robert O., Natalie Mahowald, Charlene Ung, David R. Thompson, Lori Bator, Matthew Bennet, Michael Bernas et al. "The Earth Surface Mineral Dust Source Investigation: An Earth Science Imaging Spectroscopy Mission." In 2020 IEEE Aerospace Conference, pp. 1-15. IEEE, 2020.

Guanter, L., Kaufmann, H., Segl, K., Foerster, S., Rogass, C., Chabrillat, S., Kuester, T., Hollstein, A., Rossner, G., Chlebek, C., Straif, C., Fischer, S., Schrader, S., Storch, T., Heiden, U., Mueller, A., Bachmann, M., Mühle, H., Müller, R., Habermeyer, M., Ohndorf, A., Hill, J., Buddenbaum, H., Hostert, P., Van der Linden, S., Leita˜o, P. J., Rabe, A., Doerffer, R., Krasemann, H., Xi, H., Mauser, W., Hank, T., Locherer, M., Rast, M.,

Staenz, K., and Sang, B.: The EnMAP Spaceborne Imaging Spectroscopy Mission for Earth Observation, Remote Sens., 7, 8830–8857, https://doi.org/10.3390/rs70708830, 2015.

Hakkarainen, J., Ialongo, I., Oda, T., Szelag, M. E., O'Dell, C. W., Eldering, A., and Crisp, D.: Building a bridge: Characterizing major anthropogenic point sources in the South African Highveld region using OCO-3 carbon dioxide Snapshot Area Maps and Sentinel5P/TROPOMI nitrogen dioxide columns, Environmental Research Letters, 2023.

Irons, J. R., Dwyer, J. L., and Barsi, J. A.: The next Landsat satellite: The Landsat Data Continuity Mission, Rem. Sens. Environ., 122, 11–21. https://doi.org/10.1016/j.rse.2011.08.026, 2012.

Jacob, D. J. (1999), Introduction to Atmospheric Chemistry, 280 pp., Princeton Univ. Press, Princeton, New Jersey N. J.

Joiner, J., Marchenko, S., Fasnacht, Z., Lamsal, L., Li, C., Vasilkov, A., and Krotkov, N.: Use of machine learning and principal component analysis to retrieve nitrogen dioxide (NO2) with hyperspectral imagers and reduce noise in spectral fitting, Atmos. Meas. Tech., 16, 481–500, https://doi.org/10.5194/amt-16-481-2023, 2023.

Kim, J., Jeong, U., Ahn, M.-H., Kim, J. H., Park, R. J., Lee, H., Song, C. H., Choi, Y.-S., Lee, K.-H., Yoo, J.-M., Jeong, M.-J., Park, S. K., Lee, K.-M., Song, C.-K., Kim, S.-W., Kim, Y. J., Kim, S.-W., Kim, M., Go, S., Liu, X., Chance, K., Chan Miller, C., Al-Saadi, J., Veihelmann, B., Bhartia, P. K., Torres, O., Abad, G. G., Haffner, D. P., Ko, D. H., Lee, S. H., Woo, J.-H., Chong, H., Park, S. S., Nicks, D., Choi, W. J., Moon, K.-J., Cho, A., Yoon, J., Kim, S., Hong, H., Lee, K., Lee, H., Lee, S., Choi, M., Veefkind, P., Levelt, P. F., Edwards, D. P., Kang, M., Eo, M., Bak, J., Baek, K., Kwon, H.-A., Yang, J., Park, J., Han, K. M., Kim, B.-R., Shin, H.-W., Choi, H., Lee, E., Chong, J., Cha, Y., Koo, J.-H., Irie, H., Hayashida, S., Kasai, Y., Kanaya, Y., Liu, C., Lin, J., Crawford, J. H., Carmichael, G. R., Newchurch, M. J., Lefer, B. L., Herman, J. R., Swap, R. J., Lau, A. K. H., Kurosu, T. P., Jaross, G., Ahlers, B., Dobber, M., McElroy, C. T., and Choi, Y.: New Era of Air Quality Monitoring from Space: Geostationary Environment Monitoring Spectrometer (GEMS), B. Am. Meteorol. Soc., 101, E1–E22, https://doi.org/10.1175/BAMS-D-18-0013.1, 2020.

Kim, S.-W., Heckel, A., Frost, G. J., Richter, A., Gleason, J., Burrows, J. P., McKeen, S. A., Hsie, E.-Y. Y., Granier, C., and Trainer, M. K.: NO2 columns in the western United States observed from space and simulated by a regional chemistry model and their implications for NOx emissions, J. Geophys. Res.-Atmos., 114, D11301, https://doi.org/10.1029/2008JD011343, 2009.

Kimbrough, S., Owen, R. C., Snyder, M., and Richmond-Bryant, J.: NO to NO2 Conversion Rate Analysis and Implications for Dispersion Model Chemistry Methods using Las Vegas, Nevada Near-Road Field Measurements. *Atmos. Environ.* (1994). 165:23-24. doi: 10.1016/j.atmosenv.2017.06.027.

Krotkov, N. A., Lok N. Lamsal, Sergey V. Marchenko, Edward A. Celarier, Eric J.Bucsela, William H. Swartz, Joanna Joiner and the OMI core team (2019), OMI/Aura NO2 Total and Tropospheric Column Daily L2 Global Gridded 0.25 degree x 0.25 degree V3, NASA Goddard Space Flight Center, Goddard Earth Sciences Data and Information Services Center (GES DISC), Accessed: 26 April 2023, 10.5067/Aura/OMI/DATA2018

Krings, T., Gerilowski, K., Buchwitz, M., Hartmann, J., Sachs, T., Erzinger, J., Burrows, J. P., and Bovensmann, H.: Quantification of methane emission rates from coal mine ventilation shafts using airborne remote sensing data, Atmos. Meas. Tech., 6, 151–166, https://doi.org/10.5194/amt-6-151-2013, 2013.

Lamsal, L. N., Krotkov, N. A., Vasilkov, A., Marchenko, S., Qin, W., Yang, E.-S., Fasnacht, Z., Joiner, J., Choi, S., Haffner, D., Swartz, W. H., Fisher, B., and Bucsela, E.: Ozone Monitoring Instrument (OMI) Aura nitrogen dioxide standard product version 4.0 with

improved surface and cloud treatments, Atmos. Meas. Tech., 14, 455–479, https://doi.org/10.5194/amt-14-455-2021, 2021.

Laughner, J. L. and Cohen, R. C.: Direct observation of changing NOx lifetime in North American cities, Science, 366, 723–727, https://doi.org/10.1126/science.aax6832, 2019.

Levelt, P. F., van den Oord, G. H. J., Dobber, M. R., Mälkki, A., Visser, H., de Vries, J., Stammes, P., Lundell, J., and Saari, H.: The Ozone Monitoring Instrument, IEEE T. Geosci. Remote, 44, 1093–1101, https://doi.org/10.1109/TGRS.2006.872333, 2006.

Levelt, P. F., Joiner, J., Tamminen, J., Veefkind, J. P., Bhartia, P. K., Stein Zweers, D. C., Duncan, B. N., Streets, D. G., Eskes, H., van der A, R., McLinden, C., Fioletov, V., Carn, S., de Laat, J., DeLand, M., Marchenko, S., McPeters, R., Ziemke, J., Fu, D., Liu, X., Pickering, K., Apituley, A., González Abad, G., Arola, A., Boersma, F., Chan Miller, C., Chance, K., de Graaf, M., Hakkarainen, J., Hassinen, S., Ialongo, I., Kleipool, Q., Krotkov, N., Li, C., Lamsal, L., Newman, P., Nowlan, C., Suleiman, R., Tilstra, L. G., Torres, O., Wang, H., and Wargan, K.: The Ozone Monitoring Instrument: overview of 14 years in space, Atmos. Chem. Phys., 18, 5699–5745, https://doi.org/10.5194/acp-18-5699-2018, 2018.

McFeeters, S. K.: The use of the Normalized Difference Water Index (NDWI) in the delineation of open water features, International Journal of Remote Sensing, 17:7, 1425-1432, DOI: 10.1080/01431169608948714, 1996.

Molod, A.; Takacs, L.; Suarez, M.; Bacmeister, J.; Song, I.-S.; Eichmann, A. The GEOS-5 Atmospheric General Circulation Model: Mean Climate and Development from MERRA to Fortuna; NASA TM-2012-104606; NASA, 2012.

Munro, R., Eisinger, M., Anderson, C., Callies, J., Corpaccioli, E., Lang, R., Lefebvre, A., Livschitz, Y., and Albinana, A. P. (2006). GOME-2 on MetOp. In Proceedings of the Atmospheric Science Conference 2006, SP 628. ESA, ESA, Paris.

Palmer, P. I., Jacob, D. J., Chance, K., Martin, R. V., Spurr, R. J. D., Kurosu, T. P., Bey, I., Yantosca, R., Fiore, A., and Li, Q. B.: Air mass factor formulation for spectroscopic measurements from satellites: Application to formaldehyde retrievals from the Global Ozone Monitoring Experiment, J. Geophys. Res., 106, 14 539–14 550, 2001.

Rey-Pommier, A., Chevallier, F., Ciais, P., Kushta, J., Christoudias, T., Bayram, I. S., and Sciare, J.: Detecting nitrogen oxide emissions in Qatar and quantifying emission factors of gas-fired power plants - A four-years study, EGUsphere [preprint], https://doi.org/10.5194/egusphere-2023-1024, 2023.

Schumann, U.: Large-Eddy Simulation of Turbulent Diffusion with Chemical Reactions in the Convective Boundary Layer, Atmos. Environ., 23, 1713–1727, doi:10.1016/0004-6981(89)90056-5, 1989.

Serdyuchenko, A., Gorshelev, V., Weber, M., Chehade, W., and Burrows, J. P.: High spectral resolution ozone absorption cross-sections – Part 2: Temperature dependence, Atmos. Meas. Tech., 7, 625–636, https://doi.org/10.5194/amt-7-625-2014, 2014.

Sykes, R. I., Henn, D. S., Parker, S. F., and Lewellen, W. S.: Large eddy simulation of a turbulent reacting plume, Atmos. Environ., 26A, 2565–2574, doi:10.1016/0960-1686(92)90109-X, 1992.

Tong, D.; Zhang, Q.; Davis, S. J.; Liu, F.; Zheng, B.; Geng, G. N.; Xue, T.; Li, M.; Hong, C. P.; Lu, Z. F.; Streets, D. G.; Guan, D. B.; He, K. B. Targeted emission reductions from global super-polluting power plant units. Nat. Sustain. 2018, 1, 59– 68, DOI: 10.1038/s41893-017-0003-y

U.S. Environmental Protection Agency (EPA). “Clean Air Markets Program Data.” Washington, DC: Office of Atmospheric Protection, Clean Air Markets Division. Available from EPA’s Air Markets Program Data web site: https://campd.epa.gov/.

U.S. Geological Survey (USGS): Landsat 8 (L8) Data Users Handbook. U.S. Geological Survey, Earth Resources Observation and Science Center, Sioux Falls, South Dakota, USA, 2019.

Valin, L. C., A. R. Russell, and R. C. Cohen: Variations of OH radical in an urban plume inferred from NO2 column measurements, Geophys. Res. Lett., 40, 1856–1860, doi:10.1002/grl.50267, 2013.

van Geffen, J. H. G. M., Eskes, H. J., Boersma, K. F., and Veefkind, J. P.: TROPOMI ATBD of the total and tropospheric NO_2 data products, available at: https://sentinel.esa.int/documents/247904/2476257/sentinel-5p-tropomi-atbd-no2-data-products, last access: 3 November 2022.

Vandaele, A. C., Hermans, C., Simon, P. C., Carleer, M., Colin, R., Fally, S., Mérienne, M. F., Jenouvrier, A., and Coquart, B.: Measurements of the NO2 absorption cross-section from 42 000 cm−1 to 10 000 cm−1 (238–1000 nm) at 220 K and 294 K, J. Quant. Spectrosc. Ra., 59, 171–184, https://doi.org/10.1016/S0022-4073(97)00168-4, 1998.

Varon, D. J., Jacob, D. J., McKeever, J., Jervis, D., Durak, B. O. A., Xia, Y., and Huang, Y.: Quantifying methane point sources from fine-scale satellite observations of atmospheric methane plumes, Atmos. Meas. Tech., 11, 5673–5686, https://doi.org/10.5194/amt-11-5673-2018, 2018.

Varon, D. J., Jacob, D. J., Jervis, D., and McKeever, J.: Quantifying Time-Averaged Methane Emissions from Individual Coal Mine Vents with GHGSat-D Satellite Observations, Environ. Sci. Technol., 54, 10246–10253, https://doi.org/10.1021/acs.est.0c01213, 2020.

Varon, D. J., Jervis, D., McKeever, J., Spence, I., Gains, D., and Jacob, D. J.: High-frequency monitoring of anomalous methane point sources with multispectral Sentinel-2 satellite observations, Atmos. Meas. Tech., 14, 2771–2785, https://doi.org/10.5194/amt-14-2771-2021, 2021.

Veefkind, J. P., Aben, I., McMullan, K., Förster, H., de Vries, J., Otter, G., Claas, J., Eskes, H. J., de Haan, J. F., Kleipool, Q., van Weele, M., Hasekamp, O., Hoogeveen, R., Landgraf, J., Snel, R., Tol, P., Ingmann, P., Voors, R., Kruizinga, B., Vink, R., Visser, H., and Levelt, P. F.: TROPOMI on the ESA Sentinel-5 Precursor: A GMES mission for global observations of the atmospheric composition for climate, air quality and ozone layer applications, Remote Sens. Environ., 120, 70–83, https://doi.org/10.1016/j.rse.2011.09.027, 2012.

Yang, K., Carn, S. A., Ge, C., Wang, J., and Dickerson, R. R. (2014). Advancing measurements of tropospheric NO2 from space: New algorithm and first global results from OMPS. Geophys. Res. Lett., 41:4777–4786.

Zhang, Y., Gautam, R., Zavala-Araiza, D., Jacob, D. J., Zhang, R., Zhu, L., Sheng, J.-X., and Scarpelli, T.: Satellite-Observed Changes in Mexico's Offshore Gas Flaring Activity Linked to Oil/Gas Regulations, Geophys. Res. Lett., 46, 1879–1888, https://doi.org/10.1029/2018GL081145, 2019.

Figures and Tables

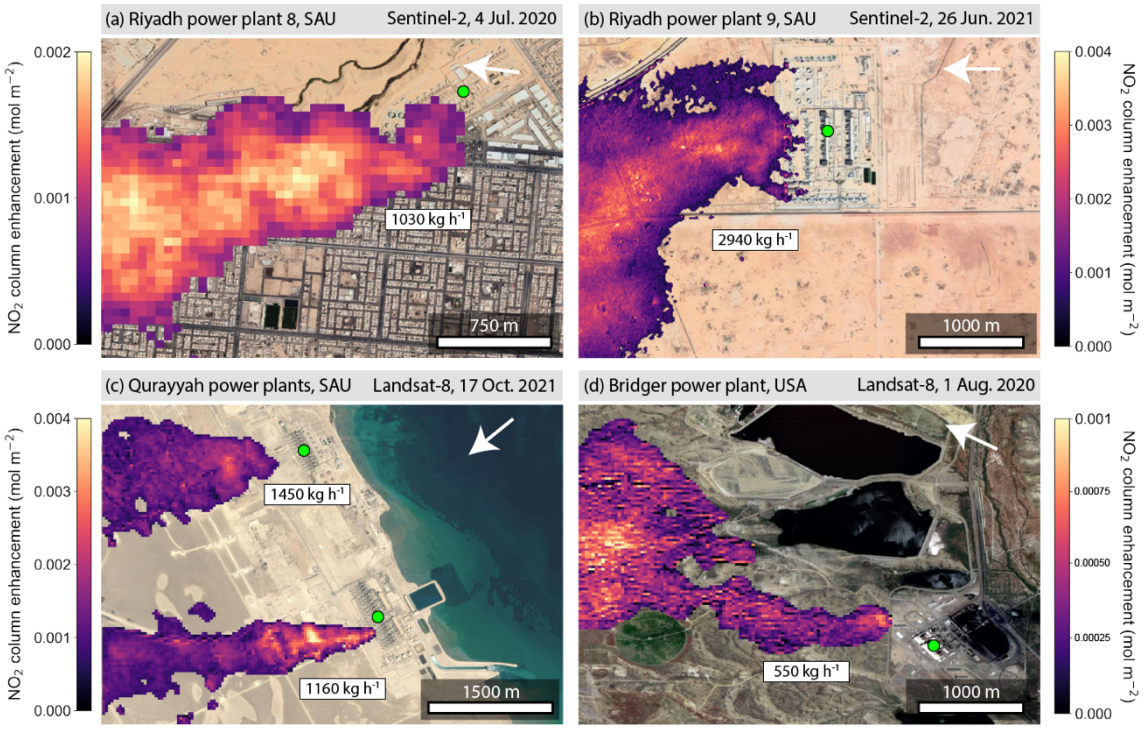

Figure 1. Sample Sentinel-2 and Landsat 8 retrievals of NO_2 plume column enhancements from five power plants in Saudi Arabia and the United States. (a) Riyadh power plant 8, Saudi Arabia (24.597°N, 46.572°E), based on the 60-m Sentinel-2 UB band. (b) Riyadh power plant 9, Saudi Arabia (24.950°N, 47.065°E), based on the 10-m Sentinel-2 B band. (c) Al-Qurrayah power plants, Saudi Arabia (25.844°N, 50.126°E). (d) Jim Bridger power plant, Wyoming, USA (41.738°N, 108.786°W). The Landsat 8 retrievals (c–d) are at 30-m resolution and based on the UB band. The white arrows indicate GEOS-FP 10-m wind direction. Inferred source rates are indicated inset. Green dots mark the emitting facilities. The color scale varies between panels.

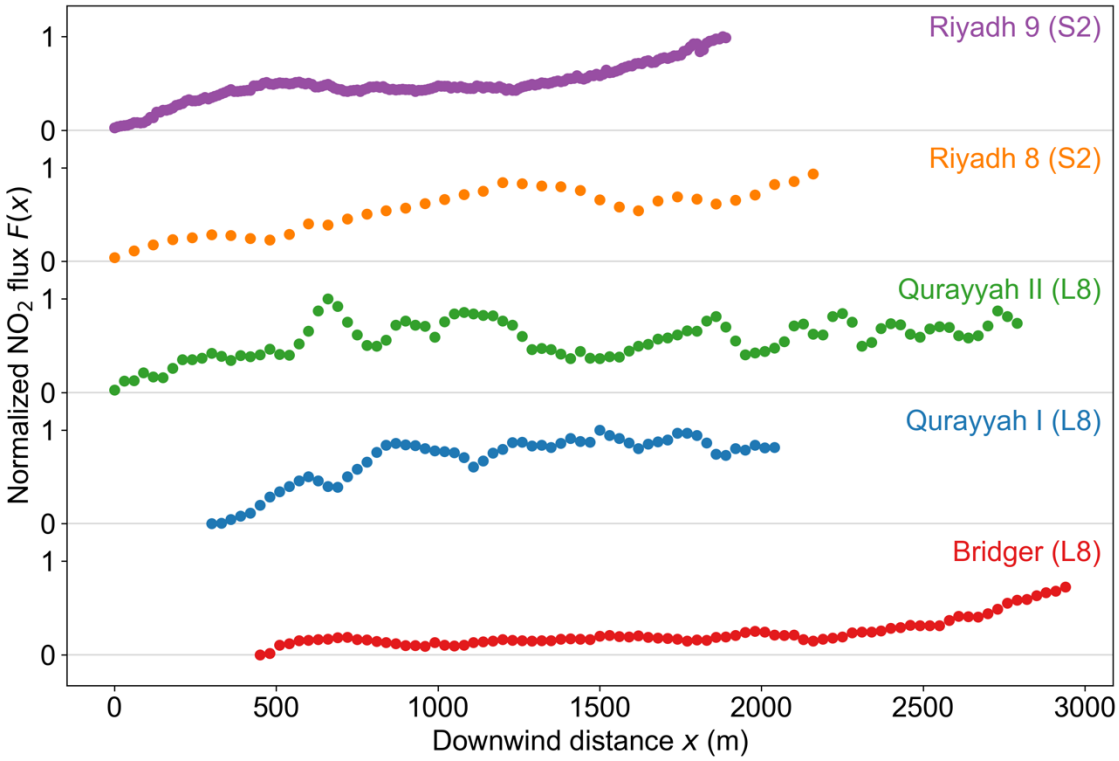

Figure 2. Normalized NO_2 flux F(x) with downwind distance *x* from the power plant for the five plumes of Figure 1. The normalization is a min-max rescaling of F(*x*) to the [0, 1] interval. The solid points represent complete plume cross-sections without truncation at the edge of the retrieval domain.

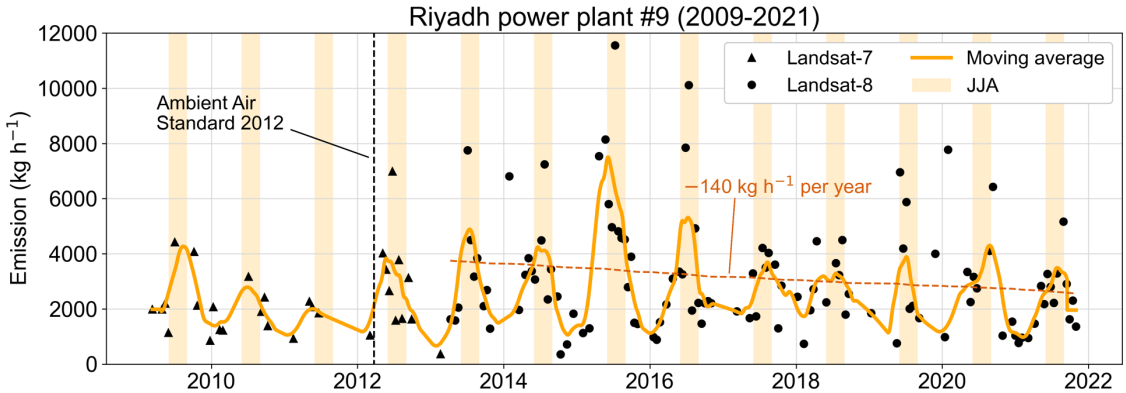

Figure 3. Time series of single-pass NO_x emissions from Riyadh power plant 9 inferred from 13 years of Landsat 7 and Landsat 8 observations from 2009 through 2021. NO_2 plumes are detectable on 30 Landsat 7 passes and 110 Landsat 8 passes. The dashed vertical line indicates the adoption of the Saudi Arabian Ambient Air Standard 2012. The orange line shows the 90-day moving average of a daily interpolation of the single-pass estimates, excluding three outliers in January 2014, January 2020, and November 2019. The dashed brown line shows the least-squares trend in emissions from 2013 through 2021. The yellow shaded regions indicate the local summer (June-July-August) months.

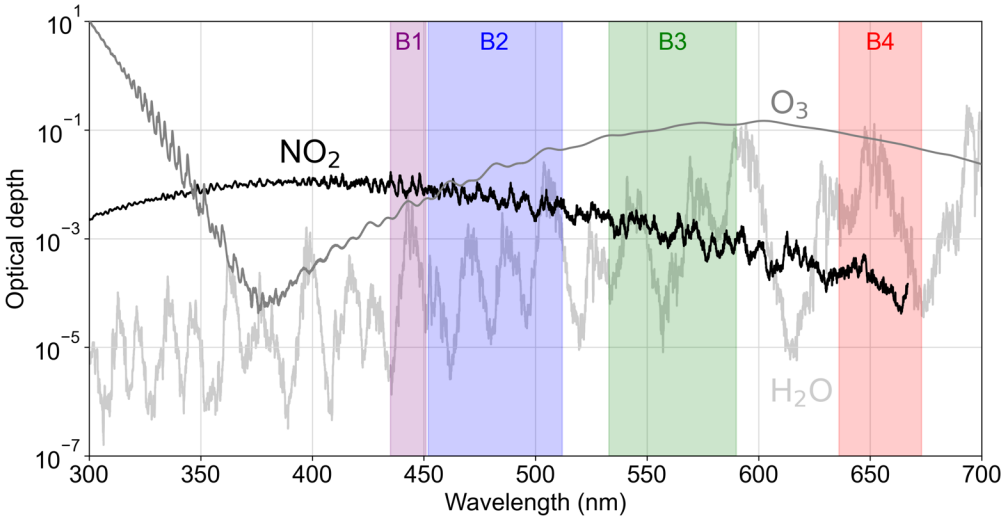

Figure 4. Slant-column optical depths of NO_2, water vapor (H_2O), and ozone (O_3) in the 300–700 nm UV/Vis spectral range, based on absorption cross-sections from Vandaele et al. (1998) for NO_2, HITRAN2016 for H_2O, and Gorshelev et al. (2014) and Serdyuchenko et al. (2014) for O_3. The optical depth calculation is performed for a solar zenith angle of 45° with nadir satellite viewing geometry and vertical profiles from the US Standard Atmosphere (Anderson et al., 1986). The shaded areas represent Landsat 8 spectral bands B1 (ultra-blue/UB, 435–451 nm), B2 (blue/B, 452–512 nm), B3 (green/G, 533–590), and B4 (red/R, 636–673 nm). Sentinel-2 has the same four bands but with slightly different positions and widths. Landsat 7 and earlier do not have the ultra-blue band but have nearly identical RGB bands.

Table 1: Comparison with previous NO_x emission estimates for the power plants of Figure 1.

	This work	Previous work	
	Estimate (kg h^{-1}) [a]	Estimate (kg h^{-1}) [b]	Source
Riyadh 8	1030	1690, 2050	Beirle et al. (2019), GPED
Riyadh 9	2750 ± 1090	2230, 3900	Beirle et al. (2019), Beirle et al. (2023)
Qurayyah I Qurayyah II	1450 1160	3310 [c]	GPED
Bridger	550	740	US EPA (CEMS) CAMPD

[a] Values are for the instantaneous plumes shown in Figure 1, except for the Riyadh 9 estimate, which is based on the Dec. 2017 – Oct. 2018 period of Figure 3.
[b] Values reflect different time periods. GPED estimates are for 2010. Estimates by Beirle et al. (2019) are for Dec. 2017 to Oct. 2018. Estimates by Beirle et al. (2023) are for 2018. The US EPA CEMS estimate is for 11:00 to 12:00 local time on 1 August 2020.
[c] Combined emission for both power plants.